Towards the Optimization of Polyurethane Aerogel Properties by Densification: Exploring the Structure–Properties Relationship

Beatriz Merillas,* Carlos A. García-González, Tomás Enrique Gómez Álvarez-Arenas, and Miguel Ángel Rodríguez-Pérez

The aerogel performance for industrial uses can be tailored using several chemical and physical strategies. The effects of a controlled densification on polyurethane aerogels are herein studied by analyzing their textural, mechanical, sound, optical, and thermal insulating properties. The produced aerogels are uniaxially compressed to different strains (30%–80%) analyzing the consequent changes in the structures and, therefore, final properties. As expected, their mechanical stiffness can be significantly increased by compression (until 55-fold higher elastic modulus for 80%-strain), while the light transmittance does not noticeably worsen until it is compressed more than 60%. Additionally, the modifications produced in the heat transfer contributions are analyzed, obtaining the optimum balance between density increase and pore size reduction. The minimum thermal conductivity (14.5%-reduction) is obtained by compressing the aerogel to 50%-strain, where the increment in the solid conduction is surpassed by the reduction of the radiative and gas contributions. This strategy avoids tedious chemical modifications in the synthesis procedure to control the final structure of the aerogels, leading to the possibility of carefully adapting their structure and properties through a simple method such as densification. Thus, it allows to obtain aerogels for current and on-demand applications, which is one of the main challenges in the field.

1. Introduction

The increasing interest by the scientific community in advanced materials is being noticeable in the last decades, being the focus of numerous research. In fact, advanced materials are considered a source of prosperity in the European Union industry as it is stated in the 2030 Advanced Materials Initiative, gathering the current challenges, objectives, and priorities, and in the Materials 2030 Manifesto.[1,2] Additionally, the Green Deal for the EU establishes the goals for a sustainable future, tackling environmental-related challenges such as reducing the greenhouse gas emissions by 60% by 2050.[3] Among the possible candidates for this purpose, aerogels are placed in a top position owing to their combination of exceptional properties that could fulfill the requirements for the settled goals. Their low density, combined with their huge porosity and surface areas, as well as their high performance as thermal and acoustic insulators, make them gather most of the main demands

B. Merillas, M. Á. Rodríguez-Pérez
Cellular Materials Laboratory (CellMat)
Condensed Matter Physics Department
Faculty of Science
University of Valladolid
Campus Miguel Delibes, Paseo de Belén 7, 47011 Valladolid, Spain
E-mail: beatriz.merillas@uva.es

B. Merillas
CERES
Department of Chemical Engineering
University of Coimbra
Rua Sílvio Lima, 3030-790 Coimbra, Portugal

The ORCID identification number(s) for the author(s) of this article can be found under https://doi.org/10.1002/sstr.202400120.

C. A. García-González
AerogelsLab
Departamento de Farmacología
Farmacia y Tecnología Farmacéutica
I+D Farma Group (GI-1645)
Facultad de Farmacia
iMATUS and Health Research Institute of Santiago de Compostela (IDIS)
Universidade de Santiago de Compostela
E-15782 Santiago de Compostela, Spain

T. E. ó. Álvarez-Arenas
Instituto de Tecnologías Físicas y de la Información, CSIC
Spanish Scientific Research Council
C/Serrano 144, 28006 Madrid, Spain

M. Á. Rodríguez-Pérez
BioEcoUVA Research Institute on Bioeconomy
University of Valladolid
47011 Valladolid, Spain

**ADVANCED
SCIENCE NEWS**

www.advancedsciencenews.com

**small
structures**

www.small-structures.com

for several sectors such as building, automotive, aeronautics, or energy management, among others.[4–6]

The current applications present each time more demanding requirements for reaching a high-performance, thus, materials should gather some specific properties to be suitable. For instance, aerogels density can be tailored by different physico-chemical modifications during the synthesis procedure, such as modifying the precursors concentration,[7] catalyst concentration,[8,9] or drying conditions.[10] However, tuning other properties such as thermal insulation, transparency, or mechanical stiffness turns into a tough task for some aerogel matrices.

Several approaches have been described in the literature for optimizing these properties in aerogel materials. For instance, their thermal insulating performance can be enhanced by the inclusion of infrared blockers, which reduce the radiative contribution, such as graphene,[11–13] titanium oxide and mineral particles,[14,15] or carbon nanotubes.[16] Nevertheless, several dispersion and heterogeneity problems usually appear in the use of this strategy. These fillers also affect the light transmittance through these materials, acting as scattering centers and, therefore, leading to transparency loss.

Regarding the mechanical properties of these materials, several approaches have been followed for increasing the mechanical strength. The developed methods range from modifying the structure through controlling the ageing step,[17] the addition of nanoparticles or fibers,[18–20] scaffolding elements,[21–23] or even polymer crosslinking.[24,25] One of the main drawbacks of the aerogels reinforcement lies on the generally increased thermal conductivity. Thus, enhancing some properties usually entails the worsening of other features, not allowing a thorough optimization.

Since the porous structure of aerogels is closely linked to their final properties, reaching tailorable characteristics requires a deep control of the reaction kinetics, precursors morphology, synthesis steps and conditions, and drying. In this work, authors analyze in detail a different strategy to modify the aerogel properties without altering their synthesis route or composition. In 2014, Weigold et al.[26] studied the correlation between the mechanical stiffness and solid conduction in a fibrillar polyurea aerogel, concluding that this correlation depends on the aerogel density. Thus, when subjecting the material to a mechanical load the aerogel skeleton changes contributing in a different way for mechanical stiffness and the solid conduction. Huang et al.[27] manipulated the porous structure of graphene-based aerogels through freeze-thaw assembly and studied its effect on their microwave absorbing performance. It was demonstrated that a controlled chemical prereduction in combination with mechanical compression (to 15, 30, and 45%), allowed to reach uniform porous structures that maximize reflection and scattering of electromagnetic waves while improving the antifrosting properties in cold and humid conditions of these materials. Therefore, this work reflects the effectiveness of modulating the aerogel's porous structure and its subsequent effect on the electromagnetic absorption. Mechanical pressing on aerogels was also applied by Wang et al.[28] with the aim of developing boron nitride aerogel films for preventing heat transfer from portable electronic devices to human skin. After compressing an aerogel slice under specific stress, authors obtained a smooth film with a high specific surface area ($624 \, \text{m}^2 \, \text{g}^{-1}$) and a high pore volume ($\approx 0.39 \, \text{cm}^3 \, \text{g}^{-1}$) that was thermally treated and dipped into organic phase change materials for an efficient heat confinement through the solid–liquid phase transition. In 2017, Plappert et al.[29] used an approach by uniaxial densification for nematic nanofibrillated 2,3-dicarboxyl cellulose aerogels. By reducing the aerogels volume down to 5% of the original volume the nematic orientation and transparency were preserved, and their toughness and stiffness were significantly increased.

However, in previous publications how compression affects other important properties such as optical, acoustic, or thermal insulating properties was not analyzed being necessary to evaluate in detail the structure–property relationship for this approach. On the basis of these results, in this research, we have applied different uniaxial compressive forces to pearl-necklace structured polyurethane-based aerogel, thus promoting a densification of the samples, which also involves the alteration of the nanoporous structure. Several levels of strain have been reached in order to evaluate the effect of the applied strain on the final structure and properties. The studied characteristics of the deformed aerogels have been textural properties, porous structure, mechanical strength, sound propagation, light transmittance, and thermal insulating performance. Moreover, a detailed theoretical study of the effect of the compression on the different heat flow contributions has been conducted, evaluating the solid and gas conduction, as well as the radiative term in order to find the optimum balance between these terms for an effective thermal superinsulation (thermal conductivities below that of the air[30]). The selection of polyurethane as aerogel matrix was based on its cost-effectiveness in combination with its low thermal conductivity that allows to reach an excellent thermal insulating performance.[31–33] Moreover, polyurethane aerogels in general reduce the brittleness inherent to most silica aerogels, constituting an interesting alternative to inorganic aerogels with growing interest.[34] In fact, some works have studied their shape-memory characteristics through temperature stimuli, and their superelasticity.[35,36] Due to their inherent mechanical performance (higher toughness than silica aerogels), it is possible to use the strategy here presented in this type of aerogels.

Thus, this study contributes to the understanding of a simple and straightforward method such as mechanical compression to tune the final properties of polyurethane aerogels, searching for the optimum combination of properties for the desired application.

2. Experimental Section

2.1. Materials

Pentaerythritol ($\rho = 1.396 \, \text{g cm}^{-3}$, purity < 98%) was used as polyol, provided by Alfa Aesar. Thermo Fisher Scientific, (Madrid, Spain), Isocyanate IsoPMDI 92 140 (p-MDI) ($\rho = 1.23 \, \text{g cm}^{-3}$), was kindly supplied by BASF Polyurethane. Kosmos 75 MEG was provided by (Evonik, Essen Germany).

Scharlab, S. L. (Barcelona, Spain) supplied all the solvents used in the synthesis: acetone (purity > 99.5%), acetonitrile (purity > 99.9%), DMSO (purity > 99.5%), and tetrahydrofurane (purity > 99.5%) stabilized with 250 ppm BHT.

2.2. Synthesis of Aerogels

Fourteen samples (two for each compression strain) of polyurethane aerogels were synthesized by polycondensation between isocyanate and polyol using a formulation previously developed by the authors.[37] A solution of isocyanate was initially prepared (44 g L^{-1} in CH$_3$CN 75% vol./THF 35% vol.) and then, the corresponding solution of pentaerythritol (100 g L^{-1} in DMSO) was added keeping a molar ratio of pol/iso = 0.43 and a 4 wt% of the catalyst (70 g L^{-1} in THF) was added (weight over the total polyol and isocyanate mass). The mixture was stirred with an electric stirrer for 20 s at 500 rpm and poured into different plastic containers. Once gels were formed, they were covered with acetonitrile and allowed to be ageing for 24 h and washed twice each 24 h with the same solvent. Finally, gels were dried by static supercritical drying at 40 °C and 100 bar in several batches of 45 min. The final aerogels were cylinders of ≈27 mm diameter, and 21 mm height.

Once the aerogels were obtained (cylinders with dimensions 28 mm diameter, 21 mm height), they were uniaxially compressed to 30, 40, 50, 60, 70, and 80% of strain by means of an universal testing machine (Instron model 5500R6025, Norwood, MA, USA). Compressions were performed at ambient conditions (23 ± 2 °C and 50 ± 10% relative humidity as indicated by ISO291:2005[38]) and at a displacement rate of (height/10) mm/min using a load cell of ≈1 kN. Despite that certain height recovery occurs (after the compression stage), samples were labeled according to the applied compression strain. This aspect is explained in more detail in **Figure 1**b.
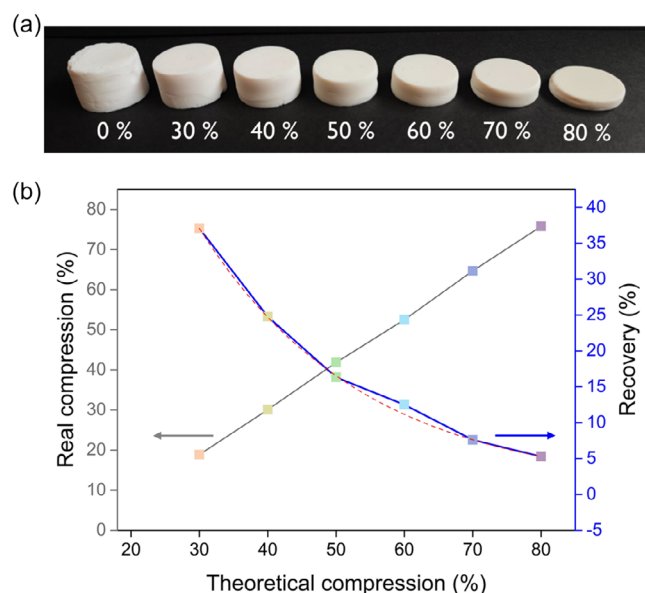

Figure 1. a) Examples of the aerogel samples under study. The original aerogel is compressed to different levels of strain to obtain the rest of samples, b) real compression and recovery percentage for all the aerogels under study.

2.3. Characterization Techniques

2.3.1. Gelation Time

During gelation, a sharp increase in density was observed accompanied by a change in color from clear yellowish to whitish. Gel time was taken at the moment that the gel does not flow by tilting the container.

2.3.2. Shrinkage

Shrinkage was measured as the difference in diameter (linear) and volume (volumetric) before and after the drying step

$$S_l(\%) = \left(1 - \frac{d}{d_0}\right) \cdot 100 \quad (1)$$

$$S_v(\%) = \left(1 - \frac{V}{V_0}\right) \cdot 100 \quad (2)$$

where d_0 and V_0 are the diameter and volume, respectively, of gels before drying, and d and V are the diameter and volume of aerogels after drying.

2.3.3. Bulk Density, Relative Density, and Porosity

Bulk density was obtained as the ratio between mass and geometrical volume as described in ASTM D1622/D1622M-14.[39] Relative density was calculated as the ratio between bulk density and the solid density of the polyurethane matrix as indicated in Equation (3)

$$\rho_r = \frac{\rho_B}{\rho_s} \quad (3)$$

where ρ_B is the geometric density and ρ_s the solid density, i.e., 1.17 g cm^{-3} measured by helium pycnometry.[37]

Porosity (Π) was measured by subtracting the solid fraction (relative density) from the unit.

2.3.4. Scanning Electron Microscopy

The structure of the obtained aerogels was observed by using a scanning electron microscope (ESEM Scanning Electron Microscope QUANTA 200 FEG, Hillsboro, OR, USA). Prior to the visualization, samples were metallized with iridium.[40]

2.3.5. Textural Properties Particle Size, Pore Volume, Pore Size and Specific Surface Area (SBET)

Nitrogen adsorption-desorption measurements were performed with a Micromeritics ASAP 2020 instrument. First, aerogels were degassed under vacuum at 25 °C for 24 h and then experiments were carried out at −196 °C in the range $P/P_0 = 0.05$–0.30. The specific surface area was obtained by the Brunauer–Emmett–Teller (BET) method.[41]

Particle size ($\varphi_{particle}$) was measured from the SEM micrographs by drawing the external shape of more than 30 particles and measuring its diameter using the Image J/FIJI software.[42]

In addition to the average particle size ($\varphi_{particle}$), the normalized standard deviation of the particle size distribution (SD/$\varphi_{particle}$) was calculated.

Pore volume was calculated as the gaseous volume per unit of mass by subtracting the solid volume from the total, as described by Equation (4)

$$V_p = \frac{1}{\rho_B} - \frac{1}{\rho_s} \tag{4}$$

Pore size was calculated using the Barrett–Joyner–Halenda (BJH) method,[41] assuming cylindrical pores

$$\Phi_{pore} = \frac{4V_p}{S_{BET}} \tag{5}$$

2.3.6. Optical Transmittance Measurements

Optical transmittance measurements were performed by using a red laser (650 nm) obtained from Laserlince S.L. (Valladolid, Spain) and an integrating sphere with 12.5 mm window (PRW0505, Gigahertz-Optik) connected to a photometer (X94, Gigahertz-Optik, Türkenfeld, Germany). Transmittance was calculated as the ratio between the intensity reaching the detector through the aerogel sample (I) and intensity emitted by the laser. Samples were placed in contact with the integrating sphere surface to avoid light intensity losses. The obtained transmittances were normalized to a selected thickness of 1 mm (L) through the following equation

$$T = T_0^{\frac{L}{L_0}} \tag{6}$$

where T_0 corresponds to the transmittance measured for a sample of thickness L_0 and L is the selected thickness to calculate the transmittance.

2.3.7. Thermal Conductivity Measurements

Thermal conductivity was measured following the steady state method through a heat flow meter model FOX 314 (TA Instruments/LaserComp, Inc.), which measures according to ASTM C518[43] and ISO 8301.[44] The method has been adapted for measuring smaller samples than the equipment sensor by means of an external heat flux sensor gSKINXM 27 9C (greenTEG AG) placed on the bottom of the sample, connected to a data logger gSKIN DLOG-4219 (greenTEG AG) as described by Sanchez-Calderón et al.[45] Measurements were performed at different temperatures (10, 20, 30, and 40 °C), with a temperature gradient between plates of 20 °C.

2.3.8. Speed of Sound Measurements

Two non-focused air-coupled ultrasonic transducers (developed at ITEFI-CSIC) were used for these measurements. Their center frequency was 250 kHz, −20 dB relative bandwidth of 75%, and 25 mm aperture. Transducers operated in transmission mode, located at a distance of 70 mm between them. The aerogel sample was placed in between at normal incidence.

Transmitter transducer is driven by a Panametrics 5077 pulser-receiver (P/R) and the received signal is amplified in the receiver stage of the 5077 (up to 40 dB) and is then transferred to a Tektronix 5054 digital oscilloscope. Finally, signal is digitized, displayed, and stored (sampling frequency 10 MS s^{-1}, record length 10 k). The oscilloscope trigger signal is provided by the 5077 P/R synchronism output signal (TTL). Ultrasound velocity in the sample (v) is calculated from the velocity in the air without sample (v_{air}), the sample thickness (d), and the difference of time of flight between the air signal and the sample signal (Δt) following Equation (7)

$$v = \frac{d}{\Delta t + d/v_{air}} \tag{7}$$

where the difference in the time of flight can be calculated from the edge detection method, the maximum in the cross-correlation between both signals, or the phase difference method.

2.3.9. Mechanical Stiffness

The elastic modulus (E) of the produced samples has been determined by the relationship between the speed of sound (v) and the bulk density as described in the Equation (8)[46]

$$v = \sqrt{\frac{E}{\rho_B}} \tag{8}$$

3. Results and Discussion

3.1. Compression Stage

The synthesized polyurethane-polyisocyanurate aerogels were compressed at strains of 30, 40, 50, 60, 70, and 80% (Figure 1a). Nevertheless, owing to certain resilience that these aerogel samples present, some height recovery occurred leading to actual strains lower than the theoretical values, as displayed in Figure 1b. Despite this recovery mechanism, a wide range of compression percentages were obtained, ranging from 18.88% to 75.78%. There is a linear correlation between the theoretical and actual strains as a result of the exponential decay tendency of the recovery percentage (red dotted line). Thus, as expected the aerogels present a higher recovery percentage for lower compression strains, that is progressively reduced when the compression strain is higher (from 37.07% of recovery for a compression of 30% until 5.27% for a compression strain of 80%).

In order to facilitate the understanding of the results, authors have maintained the theoretical compression values for labeling the samples, although the real values can be found in **Table 1**.

3.2. Aerogel Characterization

3.2.1. Density, Porosity, and Shrinkage

After the synthesis, ageing, and washing of the polyurethane gels, the 14 samples were dried by supercritical drying with

Table 1. Main properties of the produced aerogels.

Sample	ρ_B [kg m^{-3}]	ρ_R	Π [%]	Real compression [%]	Recovery [%]	S_{BET} [m^2 g^{-1}]	V_p [cm^3 g^{-1}]	Mean pore size [nm]	$\varphi_{particle}$ [nm]	SD/$\varphi_{particle}$
0%	90.3	0.077	92.30	0.00	0.00	212.0	10.22	192.85	25.79	0.268
30%	107.8	0.092	90.80	18.88	37.07	219.1	8.42	153.70	27.61	0.118
40%	124.6	0.106	89.37	30.09	24.77	218.6	7.17	131.26	25.28	0.124
50%	146.9	0.125	87.47	41.84	16.32	207.9	5.96	114.59	26.50	0.166
60%	174.5	0.149	85.11	52.50	12.51	208.0	4.88	93.78	28.33	0.197
70%	228.5	0.195	80.50	64.68	7.59	201.4	3.52	69.96	26.25	0.184
80%	313.2	0.267	73.27	75.78	5.27	195.6	2.34	47.85	23.28	0.166

ρ_B; bulk density, ρ_R; relative density, Π; porosity, S_{BET}; specific surface area, V_p; pore volume, $\varphi_{particle}$; particle size.

CO$_2$ in the same batch in order to avoid any drying differences keeping a high reproducibility between samples. The volumetric and linear shrinkages during drying were calculated being of $12.16\% \pm 1.02$ and $3.19\% \pm 0.48$, respectively having an average density of 89.24 ± 1.23 kg m^{-3}.

Once the mechanical compression was performed on the aerogel samples, bulk density, porosity, and the textural properties were measured, and gathered in Table 1.

As expected, density is significantly modified when compressing the samples. This approach led to samples from 90.3 to 313.2 kg m^{-3}, that is 347% denser samples for the highest compression strain,

following an exponential density increase as seen in **Figure 2**a. This wide range of densities led to different porosities ranging from 92.30% for the non-compressed sample to a minimum of 73.27%. At low compressions (30, 40, 50%) porosity progressively decreases to values over 85%, however, for higher compressions, porosity sharply decreases reaching the minimum value.

3.3. Porous Structures and Textural Properties

The obtained porous structures can be found in **Figure 3** for all the aerogels. It can be seen that aerogels show smaller visible
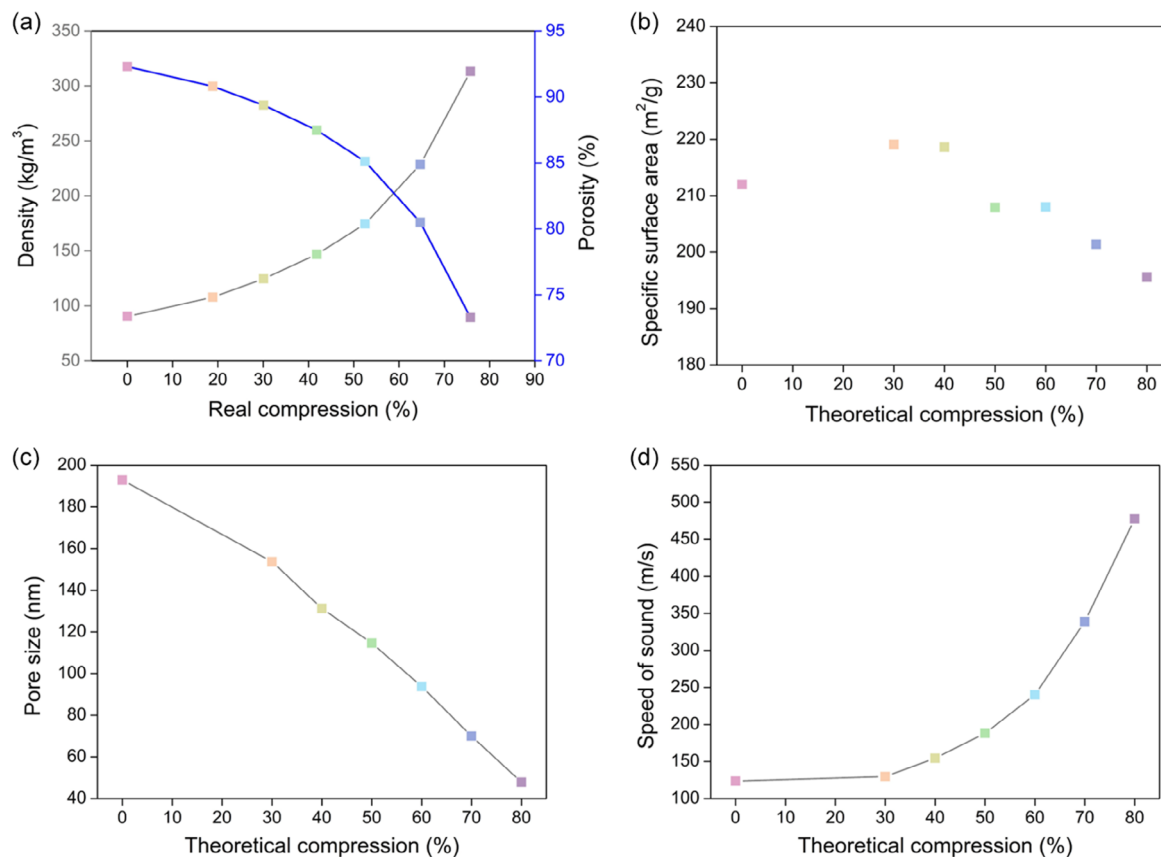

Figure 2. a) Density and porosity of the produced aerogels, b) specific surface area as a function of compression, c) pore size as a function of compression, d) speed of sound as a function of compression.
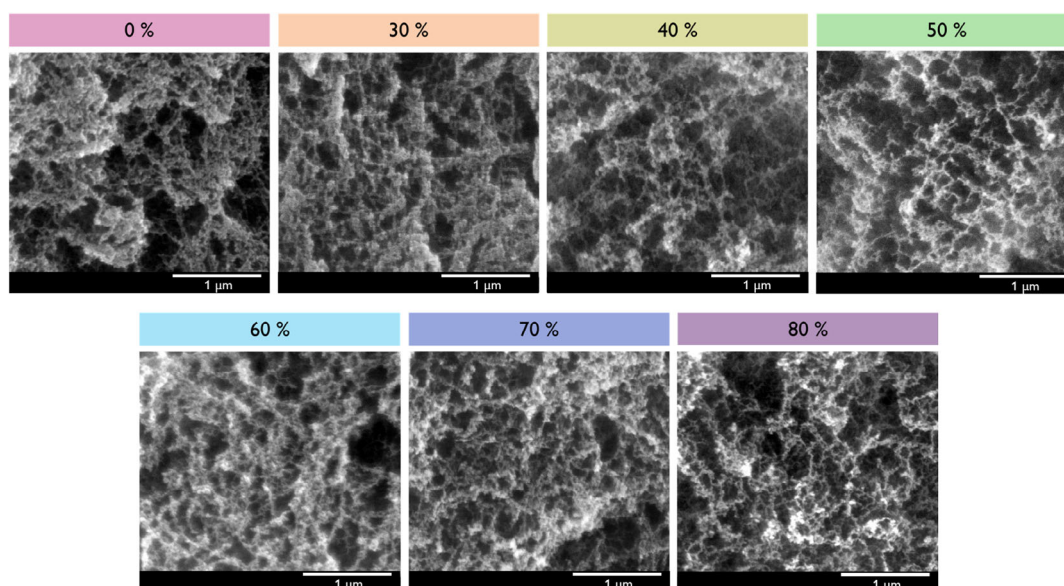
Figure 3. Scanning electron micrographs of the aerogels.

pores when being compressed, owing to the accommodation of the polymeric particles along the empty space (pores), thus increasing the packing of these particles what has a direct effect on the aerogel's density as previously seen. The structure of the aerogels was evaluated in both directions, perpendicular and parallel to compression not finding a qualitative effect in the structural features.

The effect of compression has also an influence on the specific surface areas of the samples. Although all the aerogel samples present type IV isotherms according to the IUPAC classification for mesoporous materials (Figure S1, Supporting Information),[47] it has to be noted that for a 30% and 40% of compression, the specific surface area is increased from 212.0 to 219.1 and 218.6 $m^2 g^{-1}$, respectively, thus adsorbing a higher amount of nitrogen during the experiment. This increment in the surface area is explained by Equation (5), since for low compressions pore size is being significantly reduced while the total pore volume does not experiment a proportional decrease, thus leading to higher areas. Nevertheless, when going to higher compressions, surface area is reduced to 207.9 $m^2 g^{-1}$ (50%), 208.0 $m^2 g^{-1}$ (60%), 201.4 $m^2 g^{-1}$ (70%), and 195.6 $m^2 g^{-1}$ (80%) since the total pore volume-pore size ratio is lower. This trend can be observed in Figure 2b, and data are included in Table 1. The experimented decrease in the specific surface area is not strong, confirming that compression is leading to a very narrow pore size distribution with smaller pores. Moreover, it is noticeable a shift of the capillary condensation to lower relative pressures in agreement with the reduction of pore size that is being promoted.

Then, particle and pore sizes were measured. The pore size reduction obtained during compression follows a linear trend, decreasing the pore size from 192 nm to only 48 nm (Figure 2c). Nevertheless, despite the total pore volume being decreased, there also exists a pore reorganization increasing the percentage of small mesopores with respect to the

non-compressed aerogel. **Table 2** gathers the raw values for the total pore volume and the volume that corresponds to pores between 2 and ≈100 nm corresponding to the desorption curve (BJH desorption). The percentage of macropores is measured by the difference between the total pore volume and the mesopore volume owing to the limitations of this technique to measure larger pores. Mesopores represent a 3.11% for the reference aerogel and this percentage is increased to ≈5% when compressing the aerogels to 30% and 40%, ≈7% for the one compressed at a 50%, and further increased until reach a 19% for the highest compression. The total pore volume of mesopores reaches the maximum (0.52 $cm^3 g^{-1}$) for the sample compressed until 70% and then it slightly decreases which could be due to pore-closure or the presence of very small pores that cannot be measured with this technique.

Regarding the particle size, it was proved that the average size was similar for all the samples since this feature is not being affected by the compression. The average size ranges from 23

Table 2. Pore volume and percentage of meso- and macro- pores for all the aerogels under study. V_p total pore volume was calculated as indicated in equation (4), and V_p BJH was obtained from the desorption curve.

Sample	V_p (total pore volume) [$cm^3 g^{-1}$]	V_p (BJH from desorption (2 − ≈100 nm) [$cm^3 g^{-1}$]	% mesopores (2 − ≈100 nm)	% macropores (>100 nm)
0%	10.22	0.32	3.11	96.89
30%	8.42	0.43	5.06	94.94
40%	7.17	0.39	5.46	94.54
50%	5.96	0.42	7.11	92.89
60%	4.88	0.49	10.08	89.92
70%	3.52	0.52	14.88	85.12
80%	2.34	0.45	19.42	80.58

to 28 nm being the differences in the margin of error of the measurement.

3.4. Transmittance Measurements

Light transmittance was measured with a red laser (650 nm) in order to evaluate the effect of compression on the aerogel transparency. For 1 mm of thickness, the transparency of the non-compressed aerogel was slightly increased from 70 to 71% as a direct consequence of the reduction in pore size, decreasing until 59% for the densest sample (**Figure 4**). It should be highlighted that only a 11% of transmittance is lost when compressing the aerogels at a strain of 80%, accounting for the dependence of this property with the particle size,[48] which is not modified by this processing technique.

3.5. Speed of Sound Measurements

According to the relation between the phonon transfer mechanism occurring during heat transfer through the solid phase of aerogels, and the propagation of an ultrasound wave through the particulate skeleton, the speed of sound was measured. **Table 3** gathers the time of flight calculated by different methods and the average speed of sound through the samples under study.

As displayed in Figure 2d, compression promotes a strong increase in the speed of sound through the aerogels that goes from 124 m s^{-1} for the non-compressed aerogel, to 155 m s^{-1} for the one compressed up to 40%, 339 m s^{-1} for the 70% compressed sample, reaching a maximum value of 477 m s^{-1} for the aerogel with the highest compression (almost a four-times increase). The trend followed by the speed of sound versus the compressive strain is the same followed by the density of the aerogels. Therefore, there is a huge difference in the sound wave propagation when performing a controlled compression in the aerogels, creating easier paths for the wave to travel as a result
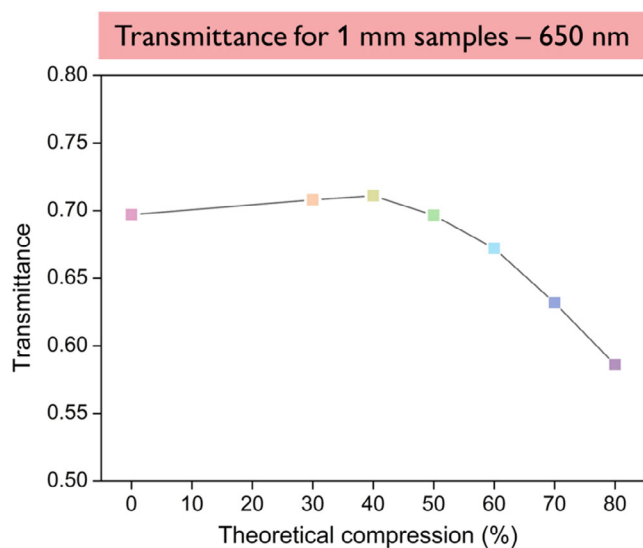
Table 3. Time of flight calculated by the edge method, cross-correlation method, and phase spectrum slope method, and the average speed of sound for the different aerogels.

Sample	Tof [µs]			Average speed of sound [m s^{-1}]
	Edge method	Cross-correlation method	Phase spectrum slope method	
0%	123.9	123.0	124.2	123.7 ± 0.6
30%	130.7	129.0	129.7	129.8 ± 0.9
40%	154.9	153.3	155.3	154.5 ± 1.1
50%	190.6	186.2	187.9	188.2 ± 2.2
60%	242.0	239.6	239.0	240.2 ± 1.6
70%	340.0	337.2	339.2	338.8 ± 1.5
80%	483.5	488.2	460.5	477.4 ± 14.8

of reducing the distances between particles, thus increasing the contact between them, and reducing the pore size. This will have a direct effect on the heat transfer by solid conduction, as it will be discussed in Section 3.7.

3.6. Mechanical Stiffness

The elastic modulus of the produced aerogels was calculated as explained in Section 2.3.10 by taking into account the aerogel density and speed of sound. A strong dependence was expected between the percentage of compression and the aerogel stiffness. The aerogel stiffness can be exponentially modulated through compression, obtaining elastic modulus ranging from 1.38 to 76.13 MPa. The lowest compressions (30, 40, and 50%) produced small increments of the elastic modulus of 1.31, 2.15, and 3.77 times in comparison with the non-compressed aerogel (**Figure 5**). When going through higher compressions, this increment reaches 7.29 times for 60%, 19.01 times for 70%, and 55.17 times for 80%. This wide range of stiffnesses expands the applicability of these materials to applications in which a structural function is necessary apart from combining other interesting properties such as transparency, high porosity and, as explained in the next section, excellent thermal insulation.

3.7. Thermal Conductivity

The thermal insulating performance of the aerogel samples was evaluated by means of the thermal conductivity measured by the steady-state method. The obtained values followed a tendency with the sample's density, as represented in **Figure 6**a. Starting with the non-compressed sample, a value of 20.25 mW m^{-1} K^{-1} was obtained at 20 °C. This value progressively decreases for the samples compressed until 30, 40, and 50% coinciding with a progressive increase in the sample density. The obtained values are 19.40, 18.27, and 17.32 mW m^{-1} K^{-1}, implying reductions of 4.2, 9.8, and 14.5%, respectively. Thus, the minimum thermal conductivity was reached for the 50%-compressed sample that showed a bulk density of 146.9 kg m^{-3}.
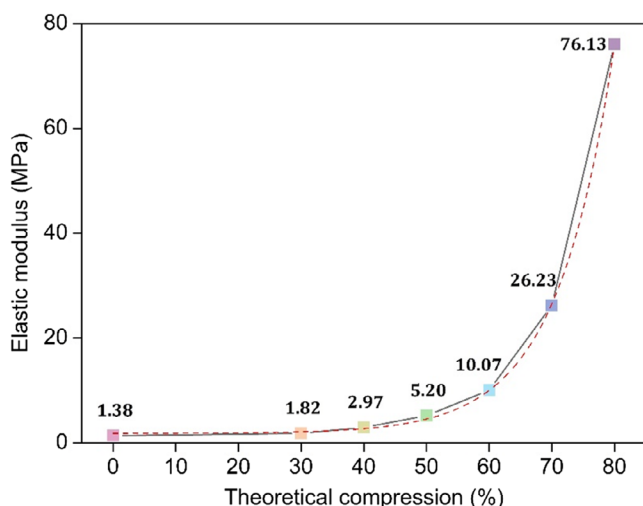

Figure 4. Light transmittance for 1 mm thick samples at a wavelength of 650 nm.

Figure 5. Elastic modulus for all the aerogels under study.

From this compression on, as density increases, thermal conductivity does too. The 60, 70, and 80% compressed samples showed thermal conductivity values of 17.76, 19.55, and 23.92 mW m^{-1} K^{-1}. Therefore, in comparison with the reference aerogel, 60% and 70% compressions still decrease the final thermal conductivity in a 12.4 and 3.5%. It is only the highest compression the one that leads to a higher thermal conductivity, with an increment of 18.1%.

The thermal conductivities measured at four different temperatures (10, 20, 30, and 40 °C) are represented in Figure 6b. It can be seen that for all aerogels thermal conductivity increases with temperature and that all the compressed samples except the 80% compressed sample show a lower thermal conductivity than the reference at all temperatures.

Aiming to understand the mechanisms behind these thermal conductivity reductions each individual heat transfer contribution has been calculated; solid conduction, gas conduction, and radiative term. The solid conduction can be described by Equation (9)

$$\lambda_s = \rho_r \cdot \lambda'_s \cdot g \tag{9}$$

where ρ_r is the relative density, λ'_s is the thermal conductivity of the solid matrix (260 mW m^{-1} K^{-1}[49]), and g is a geometrical factor that depends on the sample density. Nevertheless, in aerogels this factor is usually substituted by the ratio between the speed of sound of the aerogel and the solid matrix, being v and v_s, respectively (v/v_s). The speed of sound of solid polyurethane v_s has been taken as 1710 m s^{-1}.[50]

The gas conduction is calculated through Equation (10) in which Knudsen effect is considered since pores are in the nanometric scale for all the samples[24,51]

$$\lambda_g = (1 - \rho_r) \cdot \lambda'_g = (1 - \rho_r) \cdot \frac{\lambda'_{g0}(T)}{1 + \frac{2\beta l_g}{\phi_{pore}}} \tag{10}$$

where λ'_{g0} is the thermal conductivity of the air inside the pores (25.14 mW m^{-1} K^{-1} at 20 °C), l_g is the mean free path of the gas molecules (c.a. 70 nm for air[51,52]), β is a correlation factor (1.64 for air[53]), and φ_{pore} is the average pore size.

Since the radiative contribution (Equation (11)) involves the Rosseland extinction coefficient ($K_{e,R}$), unknown for these samples, this term has been calculated by subtracting the solid and gas contributions from the experimental values

$$\lambda_r = \frac{16 \cdot n^2 \cdot \sigma \cdot T^3}{3 \cdot K_{e,R}} \tag{11}$$

where σ is the Stephan–Boltzmann constant (5.67×10^{-8} W m^{-2} K^{-4}), n is the refractive index, and T is the mean temperature.

As it has been seen in the previous sections, compression strongly affects the final density of the aerogels, the pore size and the sound speed thus having a direct effect in the solid and gas conduction, as well as the radiation contribution.

On the one hand, the conduction through the solid backbone (**Figure 7**a) exponentially increases with density, since the phonon transfer is favored, going from values of 1.5 mW m^{-1} K^{-1} for the non-compressed aerogel, to 19.4 mW m^{-1} K^{-1} for the 80% of compression. One of the key reasons for this increase is that the geometrical factor g, that is the ratio between the aerogel speed of sound and the speed of sound of the solid material. In fact, g factor varies from 0.07 to 0.29 accounting for the stronger structural connections created during the densification step.
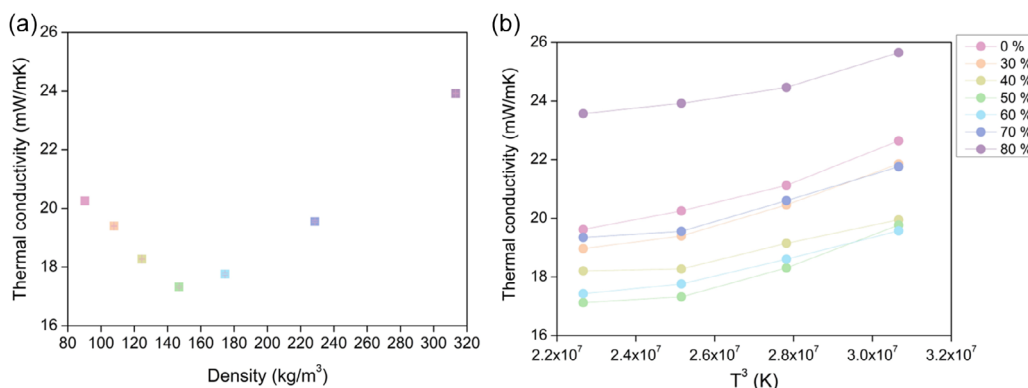

Figure 6. a) Experimental thermal conductivity values for the produced aerogels at 20 °C as a function of density, b) experimental thermal conductivities at different temperatures (10, 20, 30, and 40 °C).
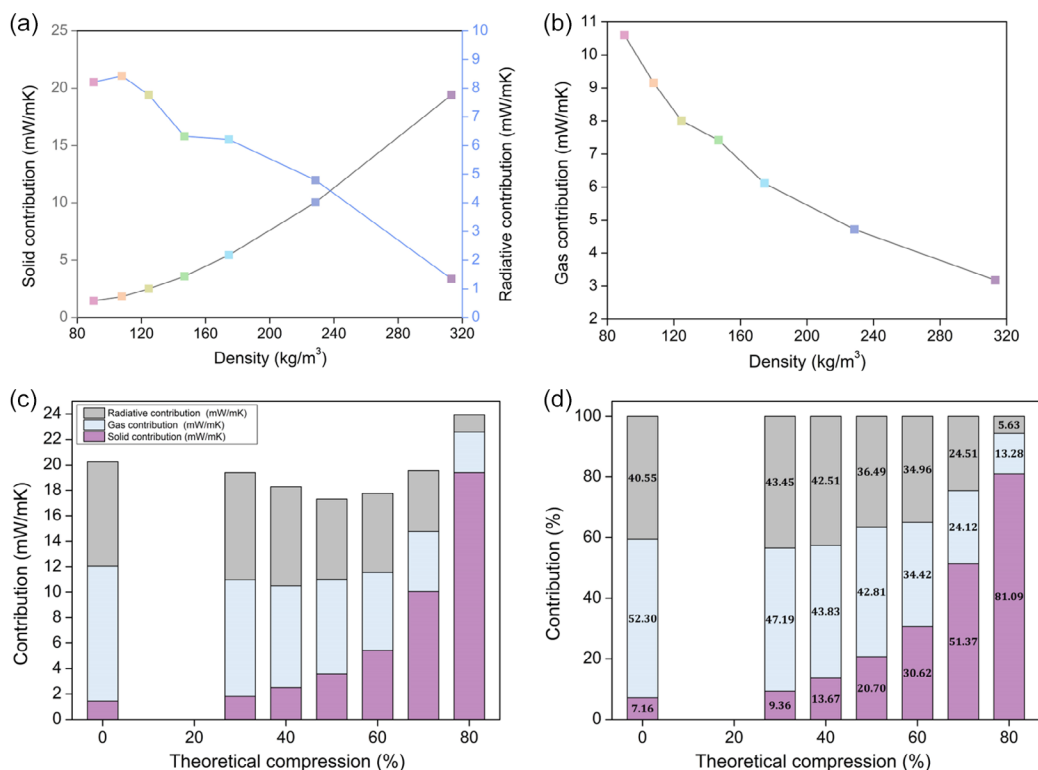
Figure 7. a) Solid and radiative contributions as a function of the sample density, b) gas contribution as a function of the sample density, c) values of each contribution of the heat transfer, d) percentage of each contribution to the total thermal conductivity. All these values are given at 20 °C.

This sharp increase in the solid conduction should significantly increment the final thermal conductivity however, density is also linked to the pore size. Thus, on the other hand, gas conduction is reduced with compression accordingly to the pore size reduction that the samples experiment during the densification. In the graph of Figure 7b, it can be observed that the non-compressed aerogel (pores of around 200 nm) led to gas conductions of $\approx 11 \text{ mW m}^{-1}\text{K}^{-1}$, value that can be reduced to only $3 \text{ mW m}^{-1}\text{K}^{-1}$ when pores are below 50 nm (sample 80%).

Finally, regarding the radiative term (values represented in Figure 7a), it is logical thinking that an increase in density would lead to a lower radiation since more absorption will be present for those materials, and this is what we observe for these samples. Aerogels with 0, 30, and 40% of compression show similar values of radiation $\approx 8 \text{ mW m}^{-1}\text{K}^{-1}$, however, when density starts to further increase, radiation is reduced to $6 \text{ mW m}^{-1}\text{K}^{-1}$ for 50% and 60% of compression and reaching only $1.4 \text{ mW m}^{-1}\text{K}^{-1}$ for the densest sample. This effect can be measured through the calculation of the Rosseland extinction coefficient $K_{e,R}$ (using Equation (11)) and its relationship with the samples density. This parameter is represented in **Figure 8**, observing its progressive increase with densification with values around 850 m^{-1} for densities between 90 and 130 kg m^{-3}, increasing to 1100 m^{-1} for densities between 140 and 180 kg m^{-3}, a higher value of 1450 m^{-1} was reached for 228 kg m^{-3}, and the maximum value of 6300 m^{-1} for the densest sample (313 kg m^{-3}).
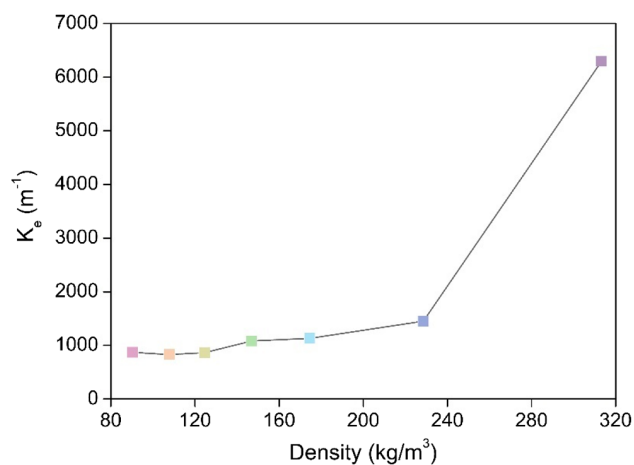

Figure 8. Extinction coefficient calculated for each aerogel sample.

The raw values for each heat transfer contribution can be found in Figure 7c.

In order to make a global comparison between samples, the percentage of each contribution has been displayed in Figure 7d. The main contribution for the un-compressed aerogel is the gas conduction that starts representing a 52%, being progressively reduced to 47, 44, 43, 34, 24, and 13% for the corresponding compressions. The same effect is observed with radiation

ADVANCED
SCIENCE NEWS
www.advancedsciencenews.com

small
structures

www.small-structures.com

Table 4. Increase and reduction percentages of the heat transfer contributions with respect to the non-compressed aerogel.

Sample	↑ Solid contribution [%]	↓ Gas contribution [%]	↓ Radiative contribution [%]
30	31	10	−7
40	91	16	−5
50	189	18	10
60	328	34	14
70	618	54	40
80	1033	75	86

decreasing from 40% to only 5% for the highest compression. On the contrary, the solid conduction is increased from 7% to 9, 13, 21, 31, 51, and 81%. **Table 4** shows the percentages of increase or reduction of the different heat conduction mechanisms for the different compressions.

The sample with the best thermal insulating performance was the one compressed until 50% (highlighted in Table 4), therefore reaching the optimum balance between contributions, being a reduction of 18% in the gas conduction, 10% in radiation, and an increase in the solid conduction of 189% with respect to the non-compressed aerogel. Thus, an initial thermal conductivity of $20.25 \, \text{mW m}^{-1} \text{K}^{-1}$ has been reduced to

$17.32 \, \text{mW m}^{-1} \text{K}^{-1}$ being placed in a really interesting region in comparison with other polyurethane-based aerogels found in the literature. **Figure 9** displays thermal conductivity values as a function of their densities for polyurethane aerogels. It can be seen that the aerogels produced in this work reach significantly low thermal conductivities ($17.32–23.92 \, \text{mW m}^{-1} \text{K}^{-1}$) covering a wide range of bulk densities ($0.09–0.31 \, \text{g cm}^{-3}$).

4. Conclusions

The effect of tuning the porous structure of a polyurethane aerogel system through a controlled compression (0, 30, 40, 50, 60, 70, and 80%) on the final structure and properties has been analyzed.

As density progressively increased with compression, a range from 90.3 to $313.2 \, \text{kg m}^{-3}$ was obtained. The study explored the impact on the textural properties finding a strong decrease in the pore size produced by the particle packaging during the densification step that decreases from 192 to 48 nm. The specific surface area was increased at low deformations as a result of reducing the pore size and then reduced from 50% deformation as a result of pore clogging.

Regarding the light transmittance at 650 nm, the initial value of ≈70% for 1 mm thickness, was not decreased for the lowest compressions (30, 40, 50%), meaning that the aerogel transparency can be maintained while a certain density increase occurs.
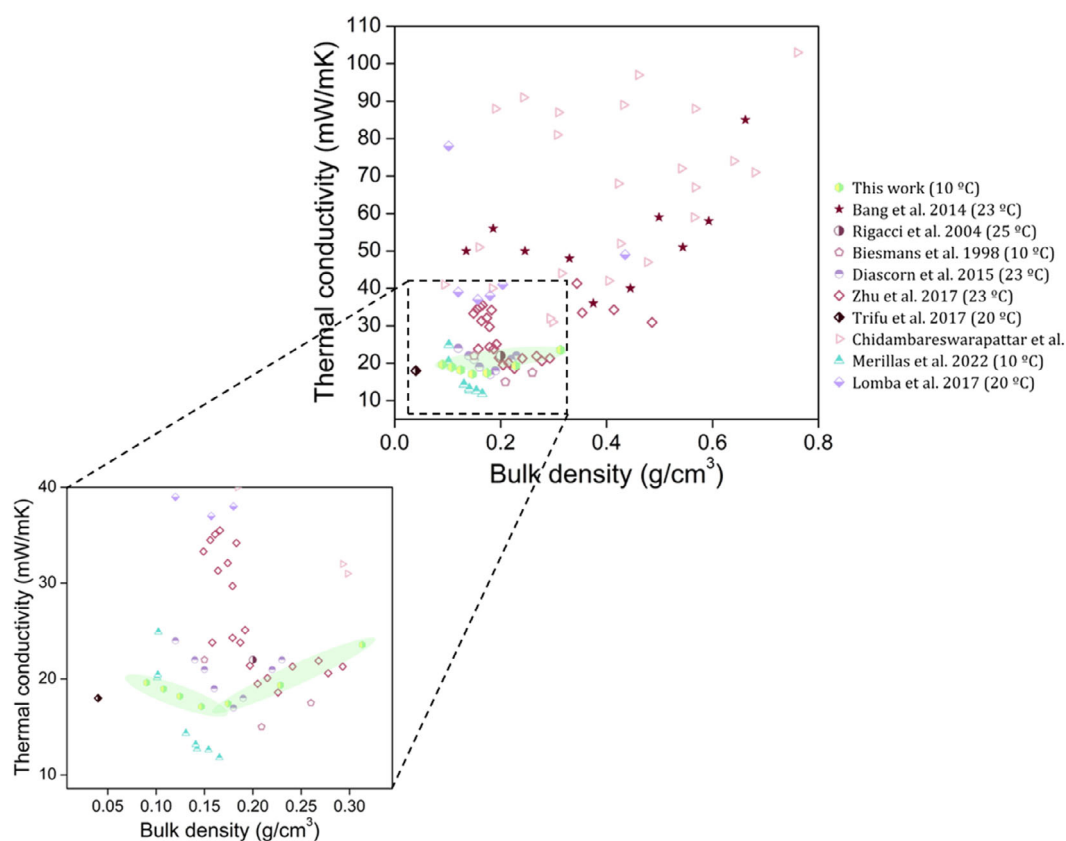

Figure 9. Thermal conductivities as a function of density found in the literature for polyurethane aerogels and those obtained in this work (highlighted in green). Ref. [9,31–33,54–58].

**ADVANCED
SCIENCE NEWS**

www.advancedsciencenews.com

**small
structures**

www.small-structures.com

Then, for higher compressions, transmittance was decreased by 59% for the largest compression (80%).

The elastic modulus shows an exponential increase with the sample density increasing from 1.38 MPa for the reference aerogel (non-compressed), to 76.13 MPa for the highest compression, implying a significant improvement on the mechanical stiffness with an increase of 55 times.

Finally, an analysis of the different heat conduction mechanisms was performed. Despite the conduction through the solid phase was progressively increased with density, this effect can be compensated with the pore size reduction and the increased Rosseland extinction coefficient, finding an optimum compression percentage of 50% in which the total thermal conductivity reaches the minimum value. Thus, the initial value of $20.25 \, \text{mW m}^{-1} \, \text{K}^{-1}$ for the non-compressed aerogel at 20 °C was reduced to $17.32 \, \text{mW m}^{-1} \, \text{K}^{-1}$, thus reducing a 14.5%, a significant percentage for aerogels that already present an excellent thermal insulating performance.

Therefore, it can be concluded that densifying aerogels through compression can be used as a straightforward strategy to modify their final properties in a controlled way reaching improvements in their transparency, stiffness, and thermal conductivity by stablishing an optimum balance between the properties of interest. Thus, this simple method can avoid several complications derived from synthesis modifications or particles and fibers inclusions, being an attractive and cost-effective alternative to modulate the aerogel properties for on-demand applications.

Supporting Information

Supporting Information is available from the Wiley Online Library or from the author.

Acknowledgements

Conflict of Interest

The authors declare no conflict of interest.

Data Availability Statement

The data that support the findings of this study are available from the corresponding author upon reasonable request.

[1] Strategic Materials Agenda, Advanced Materials Initiative 2030, **2023**.
[2] A. Cremonesi, N. Grobert, P. Gumbsch, L. Piketty, L. Montelius, K. Vandeputte, I. Vérilhac, Materials 2030 Manifesto – Systemic Approach of Advanced Materials for Prosperity, **2022**.
[3] European Commission, The European Green Deal, **2019**.
[4] S. B. Riffat, G. Qiu, *Int. J. Low-Carbon Technol.* **2013**, *8*, e1.
[5] Y. S. Kishore, *Int. Res. J. Eng. Technol.* **2020**, *7*, 5244.
[6] H. Ebert, in *Aerogels Handbook*, Springer, New York, NY, USA **2011**.
[7] X. Deng, L. Wu, Y. Deng, S. Huang, M. Sun, X. Wang, Q. Liu, M. Li, Z. Li, *J. Sol-Gel Sci. Technol.* **2021**, *100*, 477.
[8] P. B. Wagh, A. Venkateswara Rao, D. Haranath, *J. Porous Mater.* **1997**, *4*, 295.
[9] B. Merillas, F. Villafañe, M. Á. Rodríguez-Pérez, *Nanomaterials* **2022**, *12*, 2409.
[10] L. Durães, M. Ochoa, N. Rocha, R. Patrício, N. Duarte, V. Redondo, A. Portugal, *J. Nanosci. Nanotechnol.* **2012**, *12*, 6828.
[11] Y. Lei, Z. Hu, B. Cao, X. Chen, H. Song, *Mater. Chem. Phys.* **2017**, *187*, 183.
[12] L. Hong-li, H. Xiang, L. Hong-yan, L. Jing, L. Ya-jing, *Ferroelectrics* **2018**, *528*, 15.
[13] A. Lamy-Mendes, W. J. Malfait, A. Sadeghpour, A. V. Girão, R. F. Silva, L. Durães, *Carbon* **2021**, *180*, 146.
[14] J. Kuhn, T. Gleissner, M. C. Arduini-Schuster, S. Korder, J. Fricke, *J. Non-Cryst. Solids* **1995**, *186*, 291.
[15] Y. Kwon, S. Choi, *J. Mater. Sci.* **2000**, *35*, 6075.
[16] B. Merillas, T. E. Gómez Álvarez-Arenas, F. Villafañe, M. Á. Rodríguez-Pérez, *Mater. Today Chem.* **2023**, *34*, 101789.
[17] S. Iswar, W. J. Malfait, S. Balog, F. Winnefeld, M. Lattuada, M. M. Koebel, *Microporous Mesoporous Mater.* **2017**, *241*, 293.
[18] A. Karout, P. Buisson, A. Perrard, A. C. Pierre, *J. Sol-Gel Sci. Technol.* **2005**, *36*, 163.
[19] T. Linhares, V. H. Carneiro, B. Merillas, M. T. Pessoa De Amorim, L. Durães, *J. Sol-Gel Sci. Technol.* **2022**, *102*, 574.
[20] Z. Li, X. Cheng, S. He, X. Shi, L. Gong, H. Zhang, *Composites, Part A* **2016**, *84*, 316.
[21] B. Merillas, A. Lamy-Mendes, F. Villafañe, L. Durães, M. Á. Rodríguez-Pérez, *Mater. Today Chem.* **2022**, *26*, 101257.
[22] B. Merillas, A. Lamy-Mendes, F. Villafañe, L. Durães, M. Á. Rodríguez-Pérez, *Gels* **2022**, *8*, 392.
[23] A. Iglesias-Mejuto, B. Magariños, T. Ferreira-Gonçalves, R. Starbird-Pérez, C. Álvarez-Lorenzo, C. P. Reis, I. Ardao, C. A. García-González, *Carbohydr. Polym.* **2024**, *324*, 121536.
[24] M. A. Aegerter, N. Leventis, M. M. Koebel, in *Aerogels Handbook*, Springer, Berlin, Germany **2011**.
[25] H. Maleki, L. Durães, A. Portugal, *J. Non-Cryst. Solids* **2014**, *385*, 55.
[26] L. Weigold, G. Reichenauer, *J. Non-Cryst. Solids* **2014**, *406*, 73.
[27] X. Huang, G. Yu, Y. Zhang, M. Zhang, G. Shao, *Chem. Eng. J.* **2021**, *426*, 131894.
[28] B. Wang, G. Li, L. Xu, J. Liao, X. Zhang, *ACS Nano* **2020**, *14*, 16590.
[29] S. F. Plappert, J. M. Nedelec, H. Rennhofer, H. C. Lichtenegger, F. W. Liebner, *Chem. Mater.* **2017**, *29*, 6630.
[30] W. M. Haynes, in *Handbook of Chemistry and Physics*, CRC Press, Taylor & Francis Group, Boca Raton, FL **2014**.

[31] Z. Zhu, G. M. B. F. Snellings, M. M. Koebel, W. J. Malfait, *ACS Appl. Mater. Interfaces* **2017**, *9*, 18222.

[32] N. Diascorn, S. Calas, H. Sallée, P. Achard, A. Rigacci, *J. Supercrit. Fluids* **2015**, *106*, 76.

[33] G. Biesmans, D. Randall, E. Francais, M. Perrut, *J. Non-Cryst. Solids* **1998**, *225*, 36.

[34] C. Tan, B. M. Fung, J. K. Newman, C. Vu, *Adv. Mater.* **2001**, *13*, 644.

[35] S. Donthula, C. Mandal, T. Leventis, J. Schisler, A. M. Saeed, C. Sotiriou-Leventis, N. Leventis, *Chem. Mater.* **2017**, *29*, 4461.

[36] S. Malakooti, A. B. M. S. Ud Doulah, Y. Ren, V. N. Kulkarni, R. U. Soni, V. A. Edlabadkar, R. Zhang, S. L. Vivod, C. Sotiriou-Leventis, N. Leventis, H. Lu, *ACS Appl. Polym. Mater.* **2021**, *3*, 5727.

[37] B. Merillas, J. Martín-de León, F. Villafañe, M. A. Rodríguez-Pérez, *ACS Appl. Polym. Mater.* **2021**, *3*, 4607.

[38] ISO 291:2005, in *Plastics — Standard Atmospheres for Conditioning and Testing*, ISO, Geneva, Switzerland **2005**.

[39] ASTM D1622-08, in *Standard Test Method for Apparent Density of Rigid Cellular Plastics*, ASTM International, West Conshohocken, PA, USA **2008**.

[40] L. Juhász, K. Moldován, P. Gurikov, F. Liebner, I. Fábián, J. Kalmár, C. Cserháti, *Polymers* **2021**, *13*, 588.

[41] E. P. Barrett, L. G. Joyner, P. P. Halenda, *J. Am. Chem. Soc.* **1951**, *73*, 373.

[42] J. Pinto, E. Solórzano, M. A. Rodriguez-Perez, J. A. De Saja, *J. Cell. Plast.* **2013**, *49*, 555.

[43] ASTM C518, in *Standard Test Method for Steady-State Thermal Transmission Properties by Means of the Heat Flow Meter Apparatus*, ASTM International, West Conshohocken, PA, USA **2017**.

[44] ISO8301:1991, in *Thermal Insulation — Determination of Steady-State Thermal Resistance and Related Properties — Heat Flow Meter Apparatus*, ISO, Geneva, Switzerland **1991**.

[45] I. Sánchez-Calderón, B. Merillas, V. Bernardo, M. Á. Rodríguez-Pérez, *J. Therm. Anal. Calorim.* **2022**, *147*, 12523.

[46] S. Malakooti, S. Rostami, H. G. Churu, H. Luo, J. Clark, F. Casarez, O. Rettenmaier, S. Daryadel, M. Minary-Jolandan, C. Sotiriou-Leventis, N. Leventis, H. Lu, *RSC Adv.* **2018**, *8*, 21214.

[47] M. Thommes, K. Kaneko, A. V. Neimark, J. P. Olivier, F. Rodriguez-reinoso, J. Rouquerol, K. S. W. Sing, **2015**.

[48] B. Merillas, J. Martín-de León, F. Villafañe, M. Á. Rodríguez-Pérez, *Nanomaterials* **2022**, *12*, 1522.

[49] S. Estravís, J. Tirado-Mediavilla, M. Santiago-Calvo, J. L. Ruiz-Herrero, F. Villafañe, M. Á. Rodríguez-Pérez, *Eur. Polym. J.* **2016**, *80*, 1.

[50] L. W. Hrubesh, R. W. Pekala, *J. Mater. Res.* **1994**, *9*, 731.

[51] B. Notario, J. Pinto, E. Solorzano, J. A. De Saja, M. Dumon, M. A. Rodríguez-Pérez, *Polymer* **2015**, *56*, 57.

[52] C. Forest, P. Chaumont, P. Cassagnau, B. Swoboda, P. Sonntag, *Prog. Polym. Sci.* **2015**, *41*, 122.

[53] S. Song, M. M. Yovanovich, F. O. Goodman, *J. Heat Transfer* **1993**, *115*, 533.

[54] A. Bang, C. Buback, C. Sotiriou-Leventis, N. Leventis, *Chem. Mater.* **2014**, *26*, 6979.

[55] A. Rigacci, J. C. Marechal, M. Repoux, M. Moreno, P. Achard, *J. Non-Cryst. Solids* **2004**, *350*, 372.

[56] R. Trifu, G. Gould, S. White, *MRS Adv.* **2017**, *2*, 3479.

[57] C. Chidambareswarapattar, P. M. Mccarver, H. Luo, H. Lu, C. Sotiriou-leventis, N. Leventis, *Chem. Mater.* **2013**, *25*, 3205.

[58] M. Lomba, J. Garduno, E. Torres, F. Salhi, S. Bassaganas, A. Sakalyte, Organic aerogels based on isocyanate and cyclic ether polymer networks, **2017**.